

Flat-band optical phonons in twisted bilayer graphene

Emmanuele Cappelluti,¹ Jose Angel Silva-Guillén,^{2,*} Habib Rostami,^{3,4} and Francisco Guinea^{2,5,†}

¹*Istituto di Struttura della Materia, CNR (ISM-CNR), 34149 Trieste, Italy*

²*Instituto Madrileño de Estudios Avanzados, IMDEA Nanociencia, Calle Faraday 9, 28049, Madrid, Spain*

³*Department of Physics, University of Bath, Claverton Down, Bath BA2 7AY, United Kingdom*

⁴*Nordita, KTH Royal Institute of Technology and Stockholm University,
Hannes Alfvéns väg 12, 10691 Stockholm, Sweden*

⁵*Donostia International Physics Center, Paseo Manuel de Lardizábal 4, 20018,
San Sebastián, Spain; and Ikerbasque, Basque Foundation for Science, 48009, Bilbao, Spain*

Twisting bilayer sheets of graphene have been proven to be an efficient way to manipulate the electronic Dirac-like properties, resulting in flat bands at magic angles. Inspired by the electronic model, we develop a continuum model for the lattice dynamics of twisted bilayer graphene and we show that a remarkable band flattening applies to almost all the high-frequency in-plane lattice vibration modes, including the valley Dirac phonon, valley optical phonon, and zone-center optical phonon bands. Utilizing an approximate approach, we estimate small but finite magic angles at which a vanishing phonon bandwidth is expected. In contrast to the electronic case, the existence of a restoring potential prohibits the emergence of a magic angle in a more accurate modeling. The predicted phonon band-flattening is highly tunable by the twist angle and this strong dependence is directly accessible by spectroscopic tools.

Introduction. The exotic electronic, optical, and lattice properties of graphene have been enriched in the past few years by the additional possibility of manipulating two graphene layers with a finite twist angle. In twisted bilayer graphene (TBG), a complex phase diagram, including superconductivity, a Mott insulating phase, and a novel topology of the electronic bands, has been revealed [1, 2]. A key ingredient in this scenario is the existence of a non-trivial electronic structure with very narrow bandwidth, also known as flat-bands, at the so-called magic angle [3–5] has been analyzed using schemes based on either tight binding models [3, 4] or continuum models [6, 7].

Nevertheless, along with the investigation focused on the electronic properties, a large interest has also recently arisen concerning the effects of twist on the lattice dynamics. The phonon spectrum in TBG has been studied theoretically [8], and experimentally [9]. Optical [10] and acoustical [11, 12] phonons have been investigated as possible origins of the observed superconductivity. A particular high-energy optical mode at the K and K' points has been extensively studied in TBG [13–15], as it gives rise to flat moiré bands, and it couples strongly to electrons. These modes are also currently thought to be responsible for the remarkable D and 2D features in Raman spectroscopy of single-layer and multilayer graphene [16–20]. Concerning the possibility of a strong twist-driven renormalization of the phonon dispersion, calculations based on models of elastic systems have also been carried out. In Ref. [21] the emergence of a flat-band associated with out-of-plane flexural modes was shown. Similar results for the out-of-plane lattice modes were predicted for twisted “artificial” graphene systems [22]. In-plane lattice modes at the K and K' points, also characterized by Dirac physics, appear however as well, and are even

more interesting. On the one hand, these modes were initially associated with the onset of the D and 2D Raman features [23, 24]. On the other hand, the same modes, in the presence of a symmetry breaking of the sublattices as in h-BN or in transition-metal dichalcogenides (TMDs), can host chiral content that enforces fundamental selection rules [25–29]. In this scenario, it is worth mentioning that flat-bands have been also predicted in moiré structures of twisted two-dimensional TMDs [30, 31].

In this Letter, we investigate the effect of twist on the main high-energy (optical) modes at the high-symmetry points Γ and K of the phonon spectrum of TBG, with a special focus on the Dirac-like in-plane lattice modes at K. Using a force-constant (FC) model and a proper generalization of the continuum approach for the lattice phonon modes, we show that: (i) in-plane Dirac-phonons undergo upon twist a strong renormalization of the effective dispersion giving rise to flat-bands, in a similar way as Dirac-like electrons do; (ii) a “magic” angle, where the dispersion of these modes approaches zero, can be analytically predicted, and numerically observed, at twist angles remarkably larger than the ones required for the existence of flat bands in the electronic spectrum. Furthermore, we show that the appearance of flat bands is also predicted (at smaller twist angles) for the high-frequency transverse optical (TO) phonon at K and for the longitudinal-optical/transverse-optical (LO/TO) modes at the Γ point, rationalizing thus the numerical results of Ref. [13].

The model. A suitable continuum model for the lattice dynamics of TBG is derived from a FC model. Following the well-known scheme, we first construct the proper Hamiltonian for the single-layer, and for the representative limit cases of AA and AB bilayer stacking. The lattice dynamics for the twisted system is further ob-

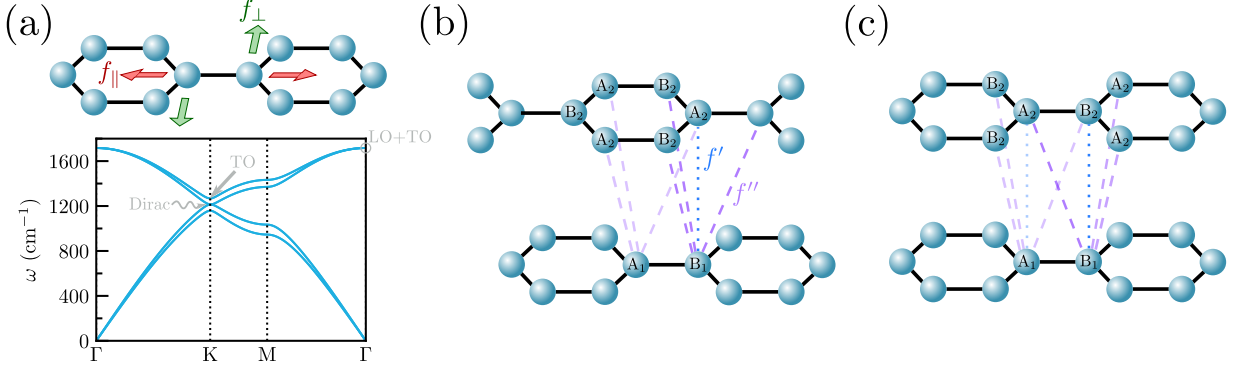


FIG. 1. Force-constant model for the untwisted cases. (a) Single-layer graphene (top) and its phonon dispersion calculated using the model. Only the elastic coupling f (solid black lines) between nearest neighbor atoms f is retained. The colored arrows denote the lattice displacements coupled with the two elastic components f_{\parallel} (red) and f_{\perp} (green). (b),(c) AB and AA bilayer graphene, respectively. The two further interlayer elastic coupling are shown, f' (dotted blue lines) and f'' (dashed purple lines).

tained by including the appropriate tunneling between a \mathbf{q} vector in one layer with a $\mathbf{q} + \mathbf{Q}_{\nu}$ vector in the other layer, where \mathbf{Q}_{ν} are the characteristic tunnelling momenta, just as for the electronic case. In order to focus on the physics of the Dirac phonons, we restrict our model to in-plane lattice displacements responsible for the Dirac modes, defining a 8-fold Hilbert basis, $u_{\alpha,i}(\mathbf{q})$, corresponding to the lattice displacements of the 4 atoms in the x - y space. Here $i = x, y$ are the Cartesian indices and $\alpha = A_1, B_1, A_2, B_2$ labels the atoms in the sublattice A, B in layer 1, 2.

The phonon band structure is thus obtained by the solution of the secular equation:

$$M \hat{\omega}^2(\mathbf{q}) \cdot \mathbf{u}(\mathbf{q}) = \hat{\mathbf{K}}(\mathbf{q}) \cdot \mathbf{u}(\mathbf{q}), \quad (1)$$

where M is the carbon mass, $\hat{\omega}^2(\mathbf{q})$ the diagonal matrix of the square frequencies, and $\hat{\mathbf{K}}(\mathbf{q})$ the dynamical matrix that takes into account the elastic couplings between different carbon atoms. In order to provide the clearest analytical insight on the manipulation of the Dirac lattice modes, we include the minimum set of FC parameters preserving the relevant physics. More explicitly, in single-layer we include elastic coupling only between in-plane nearest neighbor atoms, described by two parameters, f_{\parallel} , and f_{\perp} , ruling the relative radial and in-plane tangential lattice displacements between neighbor atoms at interatomic distance a (see Fig. 1a). The coupling between different layers in the AA and AB structure is thus described by two more kinds of elastic forces (see Figs. 1b,c): f'_{\perp} connecting vertically two atoms atop each other at the distance c ; and f'' , connecting atoms in different layers at distance $R = \sqrt{a^2 + c^2}$, with the relevant components f''_{\parallel} and f''_{\perp} , governing respectively the relative in-plane longitudinal and transverse displacement of two atoms with respect to their joining vector. The resulting dynamical matrix can thus be written as:

$$\hat{\mathbf{K}}(\mathbf{q}) = \hat{\mathbf{K}}^f(\mathbf{q}) + \hat{\mathbf{K}}^{f'}(\mathbf{q}) + \hat{\mathbf{K}}^{f''}(\mathbf{q}). \quad (2)$$

Dirac phonons at K. The Dirac phonons at the K point are more conveniently described by introducing a chiral basis $\tilde{u}_{\alpha,\nu}(\mathbf{q})$, where $\nu = R, L$ and $\tilde{u}_{\alpha,R/L} = (u_{\alpha,x} \pm i u_{\alpha,y})/\sqrt{2}$. The dynamical matrices for the AA and AB structures in this basis read:

$$\hat{\mathbf{K}}^f(\mathbf{q}) = \sum_{\nu} \hat{f}_{\nu} \hat{\sigma}_0 [\hat{\tau}_0 - \pi'_{\nu}(\mathbf{q}) \hat{\tau}_x + \pi''_{\nu}(\mathbf{q}) \hat{\tau}_y], \quad (3)$$

$$\hat{\mathbf{K}}_{AA}^{f'}(\mathbf{q}) = \hat{f}'_{\perp} [\hat{\sigma}_0 + \hat{\sigma}_x] \hat{\tau}_0, \quad (4)$$

$$\hat{\mathbf{K}}_{AB}^{f'}(\mathbf{q}) = \hat{f}'_{\perp} [\hat{\sigma}_0 \hat{\tau}_0 - \hat{\sigma}_z \hat{\tau}_z + \hat{\sigma}_x \hat{\tau}_x + \hat{\sigma}_y \hat{\tau}_y] / 2, \quad (5)$$

$$\hat{\mathbf{K}}_{AA}^{f''}(\mathbf{q}) = \sum_{\nu} \hat{f}''_{\nu} [\hat{\sigma}_0 \hat{\tau}_0 - \pi'_{\nu}(\mathbf{q}) \hat{\sigma}_x \hat{\tau}_x + i \pi''_{\nu}(\mathbf{q}) \hat{\sigma}_y \hat{\tau}_y], \quad (6)$$

$$\begin{aligned} \hat{\mathbf{K}}_{AB}^{f''}(\mathbf{q}) = & \sum_{\nu} \hat{f}''_{\nu} \{ [3 \hat{\sigma}_0 \hat{\tau}_0 - \hat{\sigma}_z \hat{\tau}_z] / 2 \\ & - \sum_{\nu} \hat{f}''_{\nu} \pi'_{\nu}(\mathbf{q}) [\hat{\sigma}_x \hat{\tau}_0 - (\hat{\sigma}_x \hat{\tau}_x - \hat{\sigma}_x \hat{\tau}_x) / 2] \\ & + \sum_{\nu} \hat{f}''_{\nu} \pi''_{\nu}(\mathbf{q}) [i \hat{\sigma}_y \hat{\tau}_0 - (\hat{\sigma}_x \hat{\tau}_y + \hat{\sigma}_y \hat{\tau}_x) / 2] \}, \end{aligned} \quad (7)$$

where $\hat{\tau}_i$ are Pauli matrices acting in the (A, B) sublattice space, $\hat{\sigma}_i$ are Pauli matrices acting in the layer space, and \hat{f}_{ν} , \hat{f}'_{ν} , \hat{f}''_{ν} are 2×2 matrices defined in the (R,L) chiral space, whose explicit expressions are reported in the Supplementary Material (SM) [32]. The index ν runs over the three vectors of the in-plane nearest neighbor B atoms with respect to an atom A, determining also the effective phonon dispersion by the non-local factors $\pi'_{\nu}(\mathbf{q}) = \text{Re}\{\exp[i\mathbf{q} \cdot \boldsymbol{\delta}_{\nu}]\}$, $\pi''_{\nu}(\mathbf{q}) = \text{Im}\{\exp[i\mathbf{q} \cdot \boldsymbol{\delta}_{\nu}]\}$, $\boldsymbol{\delta}_1 = (1, 0)$, $\boldsymbol{\delta}_2 = (-1/2, \sqrt{3}/2)$, $\boldsymbol{\delta}_3 = (-1/2, -\sqrt{3}/2)$. Note that the term $\hat{\mathbf{K}}^f(\mathbf{q})$ in the dynamical matrix does not depend on the specific AA or AB (or twisted) structure since it is purely related to intra-layer physics.

Without interlayer coupling, the phonon dispersion exhibits two degenerate Dirac cones at the K point, emerging from the longitudinal acoustic (LA) and longitudinal optical (LO) branches for each layer. In an AA struc-

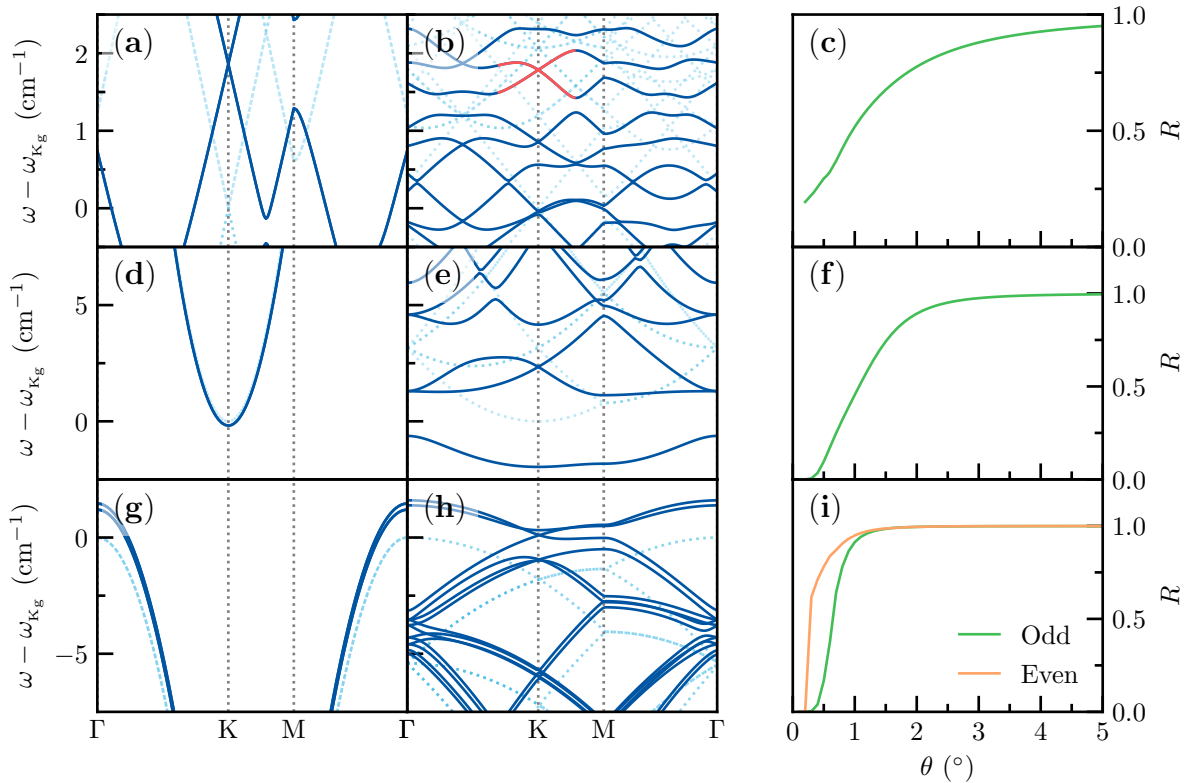


FIG. 2. Evolution with the twist angle of the phonon dispersion in the moiré Brillouin zone for the LO/LA modes at K (top panels), the TO mode at K (middle panels), and the TO modes at Γ (bottom panels). Left panels are for twist angle $\theta = 4^\circ$, central panels for $\theta = 1.05^\circ$. In panel (b) the relevant Dirac modes in the twisted cases are highlighted in red color. In the right panels we show the band renormalization factor R for each mode as a function of twist angle.

ture, these cones split into two, while only one survives in AB stacking and the other one is gapped due to the interlayer coupling. To determine the intralayer FC parameters f_{\parallel} and f_{\perp} we fix the energy of the single-layer Dirac point $\omega_0 = \sqrt{3(f_{\parallel} + f_{\perp})/2M}$, and their Dirac velocity $v = \omega_0 a(f_{\parallel} - f_{\perp})/4(f_{\parallel} + f_{\perp})$. The other interlayer elastic three parameters f'_{\perp} , f''_{\parallel} , f''_{\perp} can be determined by fixing the energies of the two Dirac cones in the AA structure, $\omega_{AA,\pm}$ [33] and by the splitting energy of the single-degenerate levels in the AB stacking $\omega_{AB,\pm}$ [32]. Using first-principles calculations [34] (see SM [32]), we obtain $f_{\parallel} = 23.882 \text{ meV/\AA}^2$, $f_{\perp} = 19.973 \text{ meV/\AA}^2$, $f'_{\perp} = -0.143 \text{ meV/\AA}^2$, $f''_{\parallel} = 0.090 \text{ meV/\AA}^2$, $f''_{\perp} = 0.059 \text{ meV/\AA}^2$.

Utilizing the dynamical matrix of two uncoupled layers and that of the AA and AB structures, we construct a continuum model in the twisted case. Here we investigate the effects of twist on the properties of few selected in-plane lattice modes, namely the Dirac phonons at the K point emerging from the LA and LO branches, the non-degenerate high-frequency TO mode at the K point. Furthermore, we study the degenerate LO and TO modes at the Γ point. For Dirac phonons, we restrict the analysis to the relevant 4-fold Hilbert sub-space containing

the left-hand chiral displacements for the A1/A2 atoms, and the right-hand chiral displacements for the B1/B2 atoms. The 4×4 dynamical matrices so obtained read:

$$\hat{\mathcal{K}}_{AA}(\tilde{\mathbf{q}}) = v\hat{\sigma}_0[\tilde{q}_x\hat{\tau}_x + \tilde{q}_y\hat{\tau}_y] + V_{AA}\hat{\sigma}_0\hat{\tau}_0 - f'_{\perp}\hat{\sigma}_x\hat{\tau}_0, \quad (8)$$

$$\hat{\mathcal{K}}_{AB}(\tilde{\mathbf{q}}) = v\hat{\sigma}_0[\tilde{q}_x\hat{\tau}_x + \tilde{q}_y\hat{\tau}_y] + V_{AB,0}\hat{\sigma}_0\hat{\tau}_0 + V_{AB,z}\hat{\sigma}_z\hat{\tau}_z - 3(f''_{\parallel} - f''_{\perp})/4[\hat{\sigma}_x\hat{\tau}_x + \hat{\sigma}_y\hat{\tau}_y], \quad (9)$$

where \tilde{q}_i are wave-vectors measured with respect to the K point and where the parameters V_{AA} , $V_{AB,0}$, $V_{AB,z}$ are ruled by the interlayer force constants (for an explicit expression see the SM [32]).

Eqs. (8)-(9) provide the basis for assessing the evolution of the Dirac phonons in TBG within a continuum model. Following a similar approach as for electrons, we describe the dynamical matrix for a twisted bilayer by interpolating the off-diagonal blocks of the AA and AB matrices in Eqs. (8)-(9) [6]. We find that the equivalent of an AA and AB interlayer tunneling are ruled by the terms:

$$t_{AA} = -f'_{\perp}/3, \quad (10)$$

$$t_{AB} = -(f''_{\parallel} - f''_{\perp})/2. \quad (11)$$

Furthermore, we notice that the diagonal elements of Eqs. (8)-(9) give rise to effective local potentials which are different for different local stackings, and hence in different regions in real space corresponding to an AA, AB or BA stacking [32]. These potentials can be expanded in reciprocal lattice vectors similarly to the way electrostatic potentials are incorporated into the continuum model for electronic bands of TBG [35]. Including in this scheme these local potentials, we show in Fig. 2a,b the evolution with the twist angle of the phonon dispersion close to the in-plane Dirac energies in the moiré Brillouin zone. We can notice an overall upward energy shift of all the phonon frequencies, stemming from the presence of such local potentials. Moreover, the phonon dispersion still shows a dispersive Dirac behavior close to K for $\theta = 4^\circ$, with a linear dispersion velocity comparable with the single-layer. Interestingly, such dispersion appears much flatter at $\theta = 1.05^\circ$, signaling a remarkable band renormalization. In order to get a qualitative estimate of a possible “phonon magic angle”, we can employ the standard approach of truncating the interlayer tunneling only to the first set of three momenta \mathbf{Q}_ν [5] and we get $\bar{\theta}_{\text{LO/LA}} \approx 2.1^\circ$ (see SM [32]). Such a picture is supported by a quantitative analysis based on multi-interlayer scattering, including local potentials. Within this framework, following Ref. [5], the flattening of the LO/LA phonon bands can be parameterized in terms of the renormalization factor $R = V^*/V$ of the Dirac phonon velocity V^* in the twisted case with respect to the one in the single-layer, V . The twist-angle dependence of R for the full multi-scattering continuum model is plotted in Fig. 2c, showing a marked depletion for twist angles $\lesssim 2^\circ$. Nevertheless, such depletion, for these as for other lattice modes, never reach a perfect flattening because of the role of the local potentials, the qualitative estimate of the phonon magic angle can properly capture the correct range of twist angles where a strong phonon band renormalization occurs.

TO phonon at K. The analysis done for Dirac phonons at K can be also extended to the TO phonon at K, which induces intervalley scattering for the electrons [13]. Following the usual scheme, the phonon wavefunction is expanded in plane waves in the two layers, where the plane wave in one layer is transferred as a superposition of three plane waves in the neighboring layer (see SM [32] for more details). The main differences with respect to the LO/LA modes are: *i*) The monolayer TO phonon is not degenerate at K, so that the spinor (sublattice) degree of freedom disappears; *ii*) The dispersion in the monolayer is quadratic in $\bar{\mathbf{q}}$. The coupling between layers includes a diagonal restoring term, which changes from the AA to the AB and BA regions, and a single interlayer coupling, which also depends on the position within the unit cell. This coupling is finite in the AA region, and it vanishes in the AB and BA regions [32]. Hence, the model includes four parameters, which can be readily ob-

tained from the FCs discussed above. The model used here resembles the ones used for the conduction band edge of MoS₂ (located at the K and K' points)[36, 37]. The representative plots of the TO phonon dispersion in the moiré Brillouin zone are shown in Fig. 2d,e, and the angle dependence of the appropriate band renormalization for the TO modes is depicted in Fig. 2f. Using the standard approximate model restricted to the first star of Bloch waves and neglecting the diagonal restoring forces, we can obtain also for these modes an estimate for the magic angle at which the prefactor of the quadratic dispersion at K vanishes [32]. We obtain $\bar{\theta}_{\text{TO}} \approx 1.0^\circ$, which is qualitatively consistent with the results shown in Fig. 2f.

Optical phonons at Γ . The continuum model for the optical phonons at Γ in TBG is particularly simplified by the fact that each plane-wave in one layer just tunnels into a single plane-wave in the other layer. As detailed in the SM [32], the interlayer forces thus couple separately the LO and the TO modes. One can further divide modes with even and odd symmetry with respect to the vertical axis. The LO and TO modes of the single-layer evolve thus in TBG into four *independent* bands with a quadratic dispersion which is ruled by different combinations of the FC parameters, and hence with four different behaviors for the band renormalization [32]. The model resembles electronic models used for the valence band edge of MoS₂ (located at the Γ point)[38–40]. The plots of the phonon dispersion of the TO modes with even and odd symmetry for different twist angles is shown in Fig. 2g,h, and the angle dependence of the effective band renormalization in Fig. 2i. Similar results (not shown) are obtained for the LO modes.

Discussion. We have analyzed the optical phonons of TBG, by introducing proper continuum models originally devised for the electronic structure. For all the three cases studied, LO/LA modes at K, TO modes at K and LO/TO modes at Γ , we find a remarkable flattening of the superlattice phonon bands at low twist angles, starting at higher values than the “magic angles” where electronic flat bands appear. The onset of such flat phonon bands is expected to tune the optical properties of TBG in the infrared frequency range, providing a possible tool for twist characterization. LO/TO modes are directly probed by one-phonon Raman and infrared spectroscopy in bilayer graphene [41], with intensities and selection rules that depend crucially on the bilayer stacking order and on the z -axis symmetry [42–46], and hence on twisting [47–50]. TO modes, and their dispersions close to the K point, are also commonly observed by means of double-resonance processes D and 2D [16–20]. Finally, although a direct contribution of the LO/LA modes at K to the Raman phonon spectroscopy is not well-assessed [16, 18, 23, 24], these modes bare a promising relevance for quantum devices since, obeying to a similar Dirac quantum-structure, they are expected to show a simi-

lar rich complexity as the electronic degree of freedom. It is also worth mentioning that the same modes in the presence of mass disproportion (e.g. in h-BN) host chiral phonon states supporting a finite lattice angular momentum [25–28], with possible application towards a suitable (lattice-based) quantum two-level systems [51, 52].

Acknowledgments All the authors thank T. Cea for useful discussions. IMDEA Nanociencia acknowledges support from the “Severo Ochoa” Programme for Centres of Excellence in R&D (CEX2020-001039-S / AEI / 10.13039/501100011033). F.G. acknowledges funding from the European Commission, within the Graphene Flagship, Core 3, grant number 881603 and from grants NMat2D (Comunidad de Madrid, Spain), SprQuMat (Ministerio de Ciencia e Innovación, Spain) and financial support through the (MAD2D-CM)-MRR MATERIALES AVANZADOS-IMDEA-NC. E.C. acknowledges financial support from PNRR MUR project PE0000023-NQSTI. H.R. acknowledges the support from the Swedish Research Council (VR Starting Grant No. 2018-04252).

Supplemental Material for: Flat-band optical phonons in twisted bilayer graphene

FORCE-CONSTANT MODEL

In this Section, we provide details about the force-constant model employed in the present paper to describe the lattice dynamics in monolayer, bilayers and twisted bilayer graphenes. We focus here only on in-plane lattice displacements that, due to their mixing of x and y component, show the most interesting physics. A similar model can be employed for out-of-plane lattice displacements.

Building blocks of such model are forces between nearest neighbor pairs of atoms connected by a vector \mathbf{r}_{ij} . Two main components can be thus identified, a parallel one with respect to \mathbf{r}_{ij} (central forces); and a perpendicular one to this vector (transverse forces) and lying in the graphene plane. A third component, orthogonal to the other two ones, can be also included, but it mainly rules the out-of-plane lattice dynamics and it does not play any relevant role in the present context.

Single-layer graphene

For an isolated graphene layer the dynamical matrix is defined in terms of the atomic lattice displacements, $\{x_A, y_A, x_B, y_B\}$, where A, B are the sublattice labels. Following the above notation, we introduce the central and transverse forces governed by the parameter f_{\parallel}, f_{\perp} respectively. The resulting 4×4 matrix reads thus:

$$H(\vec{k}) = \begin{pmatrix} H_{AA}(\vec{k}) & H_{AB}(\vec{k}) \\ H_{AB}^{\dagger}(\vec{k}) & H_{BB}(\vec{k}) \end{pmatrix}, \quad (\text{S1})$$

where

$$H_{AA}(\vec{k}) = H_{BB}(\vec{k}) = \begin{pmatrix} 3[f_{\parallel} + f_{\perp}]/2 & 0 \\ 0 & 3[f_{\parallel} + f_{\perp}]/2 \end{pmatrix}, \quad (\text{S2})$$

and

$$H_{AB}(\vec{k}) = \begin{pmatrix} 3f_{\parallel} [e_{\vec{k},a} + e_{\vec{k},b}]/4 + f_{\perp} [1 + (e_{\vec{k},a} + e_{\vec{k},b})/4] & -\sqrt{3} [f_{\parallel} - f_{\perp}] (e_{\vec{k},a} - e_{\vec{k},b})/4 \\ \sqrt{3} [f_{\parallel} - f_{\perp}] (e_{\vec{k},a} - e_{\vec{k},b})/4 & f_{\parallel} [1 + (e_{\vec{k},a} + e_{\vec{k},b})/4] + 3f_{\perp} (e_{\vec{k},a} + e_{\vec{k},b})/4 \end{pmatrix}. \quad (\text{S3})$$

Here $e_{\vec{k},i} = \exp[i\vec{k} \cdot \vec{R}_i]$ ($i = a, b$), where $\vec{R}_a = a(1/2, -\sqrt{3}/2)$, $\vec{R}_b = a(-1/2, \sqrt{3}/2)$, and $a \approx 2.46 \text{ \AA}$ is the lattice constant.

The model in Eqs. (S1)-(S3) has simple solutions at high symmetry points:

$$\begin{aligned} M\omega_{\alpha}^2(\Gamma) &= \{0, 0, 3(f_{\parallel} + f_{\perp}), 3(f_{\parallel} + f_{\perp})\}, \\ M\omega_{\alpha}^2(K) &= \left\{ 3f_{\parallel}, 3f_{\perp}, \frac{3(f_{\parallel} + f_{\perp})}{2}, \frac{3(f_{\parallel} + f_{\perp})}{2} \right\}, \\ M\omega_{\alpha}^2(M) &= \{2f_{\parallel}, 2f_{\perp}, 3f_{\parallel} + f_{\perp}, f_{\parallel} + 3f_{\perp}\}, \end{aligned} \quad (\text{S4})$$

where the index α labels the phonon branch and the parameter M is the mass of the carbon atom.

We focus on characteristic modes at the high-symmetry points Γ, K , relevant for twisted system.

The first ones are the the double-degenerate high-frequency states at the Γ point, which represent the longitudinal optical (LO) and the transverse optical (TO) modes. These modes determine the full phonon bandwidth, given by the energy

$$M\omega_{LO/TO}^2(\Gamma) = 3(f_{\parallel} + f_{\perp}). \quad (\text{S5})$$

The corresponding eigenvectors for these modes are:

$$\boldsymbol{\epsilon}_{LO/TO,x}(\Gamma) = \frac{1}{\sqrt{2}} \begin{pmatrix} 1 \\ 0 \\ -1 \\ 0 \end{pmatrix}, \quad \boldsymbol{\epsilon}_{LO/TO,y}(\Gamma) = \frac{1}{\sqrt{2}} \begin{pmatrix} 0 \\ 1 \\ 0 \\ -1 \end{pmatrix}. \quad (\text{S6})$$

Quite relevant is also the evolution of the TO branch at the K point, which leads to a the high-frequency mode at the K point, with energy

$$M\omega_{TO}^2(K) = 3f_{\parallel}, \quad (\text{S7})$$

and a typical eigenvector for transverse-optical displacements:

$$\epsilon_{TO}(K) = \frac{1}{2} \begin{pmatrix} 1 \\ -i \\ -1 \\ -i \end{pmatrix}. \quad (\text{S8})$$

The spectrum at the K point is further characterized by the doublet with energy

$$M\omega_{LO/LA}^2(K) = 3(f_{\parallel} + f_{\perp})/2. \quad (\text{S9})$$

The eigenstates for these modes at the K point can be written as:

$$\epsilon_{LO/LA,+}(K) = \frac{1}{\sqrt{2}} \begin{pmatrix} 1 \\ i \\ 0 \\ 0 \end{pmatrix}, \quad \epsilon_{LO/LA,-}(K) = \frac{1}{\sqrt{2}} \begin{pmatrix} 0 \\ 0 \\ 1 \\ -i \end{pmatrix} \quad (\text{S10})$$

The eigenstates in the K' point can be obtained by reversing the sign in front of the imaginary terms. Using such eigenstates as reduced Hilbert space, and a $\mathbf{k} \cdot \mathbf{p}$ expansion, the dynamical matrix $\tilde{\mathcal{H}}$ restricted to the closeness of the K and K' points can be thus approximated as:

$$\mathcal{H}_{LO/LA}(\vec{k}) = \begin{pmatrix} 3(f_{\parallel} + f_{\perp})/2 & Va(\xi k_x + ik_y) \\ Va(\xi k_x - ik_y) & 3(f_{\parallel} + f_{\perp})/2 \end{pmatrix} \quad (\text{S11})$$

where $\xi = \pm 1$ for the K, K' respectively. The phonon dispersion for these modes close to the K point can be written thus as:

$$E_{LO/LA}^{\pm}(\vec{k}) = M\omega_{LO/LA}^2(K) = \frac{3}{2}(f_{\parallel} + f_{\perp}) \pm Va|\vec{k}|. \quad (\text{S12})$$

The term $V = \sqrt{3}|f_{\parallel} - f_{\perp}|/4$ rules here the linear Dirac dependence of the dynamical matrix close to the K/K' point, not to be confused with the linear slope of the phonon dispersion.

Graphene bilayers.

The force-constant model described above for single-layer graphene can be extended in a compelling way to graphene bilayers. We analyze in details in the following the AA and the AB stacking structures, whereas the model for BA stacking can be obtained from the AB by switching the sublattice space indices. We include interlayer force constants only up to the second nearest neighbors carbon pairs. In both cases interlayer nearest neighbors are represented by carbon atoms lying directly on top of each other, at the interlayer distance, $d \approx 3.4\text{\AA}$. The only elastic term between these atoms is the transverse one, ruled by f'_{\perp} . Second interlayer nearest neighbors are represented by atoms at the interatomic distance $\sqrt{d^2 + a^2}/3 \approx 3.5\text{\AA}$. In the case both the two parallel and transverse components need to be taken into account, parametrized by the terms $f''_{\parallel}, f''_{\perp}$.

Using the 8-fold spinor represented by the lattice displacements for both layers, for a generic bilayer graphene system, the dynamical matrix can be written as:

$$H^{2L}(\vec{k}) = H^{1L+1L}(\vec{k}) + \delta H(\vec{k}), \quad (\text{S13})$$

where $H^{1L+1L}(\vec{k})$ is the dynamical matrix for the two decoupled layers and $\delta H(\vec{k})$ takes into account the interlayer forces. It is clear that 8×8 $H^{1L+1L}(\vec{k})$ can be written as a block-diagonal matrix,

$$H^{1L+1L}(\vec{k}) = \begin{pmatrix} H(\vec{k}) & 0 \\ 0 & H(\vec{k}) \end{pmatrix}, \quad (\text{S14})$$

whereas

$$\delta H(\vec{k}) = \begin{pmatrix} \delta H_{11}(\vec{k}) & \delta H_{12}(\vec{k}) \\ \delta H_{12}^\dagger(\vec{k}) & \delta H_{22}(\vec{k}) \end{pmatrix}, \quad (\text{S15})$$

which contains both block on-diagonal terms, resulting from the quadratic elastic contributions associated with a single-atom lattice displacements, and block off-diagonal terms which describe the effective interlayer elastic forces.

More explicitly, for the AA and AB structures we have respectively:

$$\delta H_{11}^{AA}(\vec{k}) = \delta H_{22}^{AA}(\vec{k}) = \begin{pmatrix} f'_\perp + \frac{3(f''_\parallel + f''_\perp)}{2} & 0 & 0 & 0 \\ 0 & f'_\perp + \frac{3(f''_\parallel + f''_\perp)}{2} & 0 & 0 \\ 0 & 0 & f'_\perp + \frac{3(f''_\parallel + f''_\perp)}{2} & 0 \\ 0 & 0 & 0 & f'_\perp + \frac{3(f''_\parallel + f''_\perp)}{2} \end{pmatrix}, \quad (\text{S16})$$

and

$$\delta H_{11}^{AB}(\vec{k}) = \begin{pmatrix} f'_\perp + \frac{3(f''_\parallel + f''_\perp)}{2} & 0 & 0 & 0 \\ 0 & f'_\perp + \frac{3(f''_\parallel + f''_\perp)}{2} & 0 & 0 \\ 0 & 0 & 3(f''_\parallel + f''_\perp) & 0 \\ 0 & 0 & 0 & 3(f''_\parallel + f''_\perp) \end{pmatrix}$$

$$\delta H_{\vec{k}}^{AB,22} = \begin{pmatrix} 3(f''_\parallel + f''_\perp) & 0 & 0 & 0 \\ 0 & 3(f''_\parallel + f''_\perp) & 0 & 0 \\ 0 & 0 & f'_\perp + \frac{3(f''_\parallel + f''_\perp)}{2} & 0 \\ 0 & 0 & 0 & f'_\perp + \frac{3(f''_\parallel + f''_\perp)}{2} \end{pmatrix} \quad (\text{S17})$$

In similar way, the interlayer forces for a generic bilayer structures read:

$$\delta H_{12}^\alpha(\vec{k}) = \begin{pmatrix} \delta H_{12,AA}^\alpha(\vec{k}) & \delta H_{12,AB}^\alpha(\vec{k}) \\ \delta H_{12,BA}^\alpha(\vec{k}) & \delta H_{12,BB}^\alpha(\vec{k}) \end{pmatrix}. \quad (\text{S18})$$

Note that here the upper label $\alpha = AA, AB$ denotes the stacking order, whereas the indices AA, AB in the subscript represent the sublattice label for each layer. Using these notations, we obtain:

$$\delta H_{12,AA}^{AA}(\vec{k}) = \delta H_{12,BB}^{AA}(\vec{k}) = \begin{pmatrix} -f'_\perp & 0 \\ 0 & -f'_\perp \end{pmatrix}, \quad (\text{S19})$$

$$\delta H_{12,AB}^{AA}(\vec{k}) = \delta H_{12,AB}^{AA}(\vec{k})$$

$$= \begin{pmatrix} -\frac{3}{4}f''_\parallel (e_{\vec{k},a} + e_{\vec{k},b}) + \frac{f''_\perp}{4} [1 + (e_{\vec{k},a} + e_{\vec{k},b})] & \frac{\sqrt{3}}{4} [f''_\parallel - f''_\perp] (e_{\vec{k},a} - e_{\vec{k},b}) \\ \frac{\sqrt{3}}{4} [f''_\parallel - f''_\perp] (e_{\vec{k},a} - e_{\vec{k},b}) & \frac{3}{4}f''_\parallel (e_{\vec{k},a} + e_{\vec{k},b}) + \frac{f''_\perp}{4} [1 + (e_{\vec{k},a} + e_{\vec{k},b})] \end{pmatrix} \quad (\text{S20})$$

$$\delta H_{12,AA}^{AB}(\vec{k}) = \delta H_{12,BB}^{AB}(\vec{k})$$

$$= \begin{pmatrix} -\frac{3}{4}f''_\parallel (e_{\vec{k},a}^* + e_{\vec{k},b}^*) - \frac{f''_\perp}{4} [1 + (e_{\vec{k},a}^* + e_{\vec{k},b}^*)] & \frac{\sqrt{3}}{4} [f''_\parallel - f''_\perp] (-e_{\vec{k},a}^* + e_{\vec{k},b}^*) \\ \frac{\sqrt{3}}{4} [f''_\parallel - f''_\perp] (-e_{\vec{k},a}^* + e_{\vec{k},b}^*) & -\frac{3}{4}f''_\parallel (e_{\vec{k},a}^* + e_{\vec{k},b}^*) - \frac{f''_\perp}{4} [1 + (e_{\vec{k},a}^* + e_{\vec{k},b}^*)] \end{pmatrix} \quad (\text{S21})$$

$$\delta H_{12,AB}^{AB}(\vec{k}) = \begin{pmatrix} -f'_\perp & 0 \\ 0 & -f'_\perp \end{pmatrix}, \quad (\text{S22})$$

$$\delta H_{12,BA}^{AB}(\vec{k}) = \begin{pmatrix} -\frac{3}{4}f''_\parallel(e_{\vec{k},a}^* + e_{\vec{k},b}^*) - \frac{f''_\perp}{4} [e_{\vec{k},a}^* e_{\vec{k},b}^* + (e_{\vec{k},a}^* + e_{\vec{k},b}^*)] & -\frac{\sqrt{3}}{4}[f''_\parallel - f''_\perp](e_{\vec{k},a}^* - e_{\vec{k},b}^*) \\ -\frac{\sqrt{3}}{4}[f''_\parallel - f''_\perp](e_{\vec{k},a}^* - e_{\vec{k},b}^*) & -\frac{3}{4}f''_\parallel(e_{\vec{k},a}^* + e_{\vec{k},b}^*) - \frac{f''_\perp}{4} [e_{\vec{k},a}^* e_{\vec{k},b}^* + (e_{\vec{k},a}^* + e_{\vec{k},b}^*)] \end{pmatrix} \quad (\text{S23})$$

On the ground of the knowledge of the full dynamical matrix for generic branch and generic momentum, we can now build up the effective model for selected modes in the bilayer structures, in the spirit of a $\mathbf{k} \cdot \mathbf{p}$ expansion.

Dirac LO/LA modes at K point

We first address the LO/LA modes at the K point, which gives rise to a linear Dirac-like phonon dispersion.

Using the eigenstates (S10) in each layer, we can write the effective dynamical matrix for a bilayer with generic structure $\alpha = AA, AB$ in a reduced 4×4 Hilbert space:

$$\mathcal{H}_{LO/LA}^\alpha(\vec{k}) = \begin{pmatrix} \mathcal{H}_{LO/LA}(\vec{k}) + \mathcal{V}_{LO/LA,1}^\alpha & \mathcal{H}_{LO/LA,12}^\alpha \\ \mathcal{H}_{LO/LA,12}^{\alpha,\dagger} & \mathcal{H}_{LO/LA}(\vec{k}) + \mathcal{V}_{LO/LA,2}^\alpha \end{pmatrix}, \quad (\text{S24})$$

where $\mathcal{H}_{LO/LA}(\vec{k})$ is the $\mathbf{k} \cdot \mathbf{p}$ expansion for the LO/LA modes at the K point for a single-layer, as reported in Eq. (S11), $\mathcal{H}_{LO/LA,12}^\alpha$ is the 2×2 interlayer coupling matrix which is different for different stacking orders, namely:

$$\mathcal{H}_{LO/LA,12}^{AA} = \begin{pmatrix} -f'_\perp & 0 \\ 0 & -f'_\perp \end{pmatrix}, \quad (\text{S25})$$

$$\tilde{\mathcal{H}}_{LO/LA,12}^{AB} = \begin{pmatrix} 0 & 0 \\ -\frac{3}{2}(f''_\parallel - f''_\perp) & 0 \end{pmatrix}, \quad (\text{S26})$$

and where $\mathcal{V}_{LO/LA,i}^\alpha$ are 2×2 diagonal matrices that represent the stacking-dependent onsite intra-atomic potential on each layer $i = 1, 2$ due to interlayer elastic coupling, explicitly:

$$\mathcal{V}_{LO/LA,1}^{AA} = \mathcal{V}_{LO/LA,2}^{AA} = \begin{pmatrix} f'_\perp + \frac{3}{2}(f''_\parallel + f''_\perp) & 0 \\ 0 & f'_\perp + \frac{3}{2}(f''_\parallel + f''_\perp) \end{pmatrix}, \quad (\text{S27})$$

$$\mathcal{V}_{LO/LA,1}^{AB} = \begin{pmatrix} \frac{3}{2}(f''_\parallel + f''_\perp) + f'_\perp & 0 \\ 0 & 3(f''_\parallel + f''_\perp) \end{pmatrix}, \quad (\text{S28})$$

$$\mathcal{V}_{LO/LA,2}^{AB} = \begin{pmatrix} 3(f''_\parallel + f''_\perp) & 0 \\ 0 & \frac{3}{2}(f''_\parallel + f''_\perp) + f'_\perp \end{pmatrix}. \quad (\text{S29})$$

The corresponding frequencies at the K point for each stacking structure read thus:

$$M\omega_{LO/LA,AA}^2(K) = \begin{cases} \frac{3}{2}(f_\parallel + f_\perp) + 2f'_\perp + \frac{3}{2}(f''_\parallel + f''_\perp) & \text{(double degenerate),} \\ \frac{3}{2}(f_\parallel + f_\perp) + \frac{3}{2}(f''_\parallel + f''_\perp) & \text{(double degenerate),} \end{cases} \quad (\text{S30})$$

$$M\omega_{LO/LA,AB}^2(K) = \begin{cases} \frac{3}{2}(f_\parallel + f_\perp) + f'_\perp + \frac{3}{2}(f''_\parallel + f''_\perp) & \text{(double degenerate),} \\ \frac{3}{2}(f_\parallel + f_\perp) + \frac{3}{2}(3f''_\parallel + f''_\perp), & \\ \frac{3}{2}(f_\parallel + f_\perp) + \frac{3}{2}(f''_\parallel + 3f''_\perp), & \end{cases} \quad (\text{S31})$$

Note that, in the AA stacking, the first state corresponds to out-of-phase lattice displacements in the two layers, whereas the second frequency described in-phase in-plane lattice vibrations.

In similar way as for the electronic structure, the interlayer coupling gives rise thus to different effects according to the different stacking. More in particular, in strict similarity with the electronic dispersion, the Dirac-like LO/LA modes at the K point of the single-layer gives rise in the AA bilayer to two Dirac phonon cones split by the interlayer coupling; while in the AB structure just one Dirac phonon cone survives (check) whereas the other one is effectively gapped.

High-energy TO modes at K point

An effective $\mathbf{k} \cdot \mathbf{p}$ model can be built also for the high-energy TO mode at the K point. Starting point is this case will be the eigenstate $\epsilon_{TO}(K)$ as expressed in Eq. (S8). Using such state in each layer, we can build up a 2×2 $\mathbf{k} \cdot \mathbf{p}$ model close to the K point for these modes in the bilayer systems as:

$$\mathcal{H}_{TO,K}^\alpha(\vec{k}) = \begin{pmatrix} \mathcal{H}_{TO,K}(\vec{k}) + \mathcal{V}_{TO,K}^\alpha & \mathcal{H}_{TO,K}^\alpha \\ \mathcal{H}_{TO,K}^\alpha & \mathcal{H}_{TO,K}(\vec{k}) + \mathcal{V}_{TO,K}^\alpha \end{pmatrix}, \quad (\text{S32})$$

where $\mathcal{H}_{TO,K}(\vec{k})$ is the dynamical matrix at the quadratic order of this mode in the single-layer,

$$\mathcal{H}_{TO,K}(\vec{k}) = 3f_{\parallel} + \frac{f_{\parallel}f_{\perp}}{2(f_{\parallel} - f_{\perp})}(k_x^2 + k_y^2)a^2, \quad (\text{S33})$$

$\mathcal{H}_{TO,K}^\alpha$ is the inter-layer coupling,

$$\mathcal{H}_{TO,K}^{AA} = -f'_{\perp} + \frac{3(f''_{\parallel} - f''_{\perp})}{2}, \quad (\text{S34})$$

$$\mathcal{H}_{TO,K}^{AB} = 0, \quad (\text{S35})$$

and $\mathcal{V}_{TO,K}^\alpha$ represents the onsite intra-atomic potential:

$$\mathcal{V}_{TO,K}^{AA} = f'_{\perp} + \frac{3(f''_{\parallel} + f''_{\perp})}{2}, \quad (\text{S36})$$

$$\mathcal{V}_{TO,K}^{AB} = \frac{f'_{\perp}}{2} + \frac{9(f''_{\parallel} + f''_{\perp})}{4}. \quad (\text{S37})$$

Such analysis shows that the high-frequency TO modes at the K point in the AB structure remain degenerate with a resulting frequency

$$M\omega_{TO,AB}^2(K) = 3f_{\parallel} + \frac{1}{2}f'_{\perp} + \frac{9}{4}(f''_{\parallel} + f''_{\perp}) \quad (\text{double degenerate}), \quad (\text{S38})$$

whereas the interlayer coupled leads to a lift of the degeneracy in the AA stacking, resulting in the frequencies

$$M\omega_{TO,AA}^2(K) = \begin{cases} 3f_{\parallel} + 3f''_{\parallel}, \\ 3f_{\parallel} + 2f'_{\perp}3f''_{\perp}. \end{cases} \quad (\text{S39})$$

High-energy LO/TO modes at the Γ point

Finally, an effective $\mathbf{k} \cdot \mathbf{p}$ model can be built also for the high-energy LO/TO modes at the Γ point. Since the single-layer shows two degenerate modes at the Γ point, also in this case the effective model will be described by a 4×4 dynamical matrix resulting by the interlayer coupling of 2×2 blocks in each layer. We can thus write:

$$\mathcal{H}_{LO/TO,\Gamma}^\alpha(\vec{k}) = \begin{pmatrix} \mathcal{H}_{LO/TO,\Gamma}(\vec{k}) + \mathcal{V}_{LO/TO,\Gamma}^\alpha & \mathcal{H}_{LO/TO,\Gamma}^\alpha \\ \mathcal{H}_{LO/TO,\Gamma}^{\alpha,\dagger} & \mathcal{H}_{LO/TO,\Gamma}(\vec{k}) + \mathcal{V}_{LO/TO,\Gamma}^\alpha \end{pmatrix}, \quad (\text{S40})$$

where $\mathcal{H}_{LO/TO,\Gamma}(\vec{k})$ is the dynamical matrix at the quadratic order for the single-layer:

$$\mathcal{H}_{LO/TO,\Gamma}(\vec{k}) = \begin{pmatrix} 3(f_{\parallel} + f_{\perp}) - \frac{f_{\perp}(3f_{\parallel} + f_{\perp})}{8(f_{\parallel} + f_{\perp})}|\vec{k}|^2 & 0 \\ 0 & 3(f_{\parallel} + f_{\perp}) - \frac{f_{\parallel}(f_{\parallel} + 3f_{\perp})}{8(f_{\parallel} + f_{\perp})}|\vec{k}|^2 \end{pmatrix}, \quad (\text{S41})$$

$\mathcal{H}_{LO/TO,\Gamma}^\alpha$, as usual, is the 2×2 interlayer coupling for each stacking order:

$$\mathcal{H}_{LO/TO,\Gamma}^{AA} = \begin{pmatrix} -f'_\perp + \frac{3(f''_\parallel + f''_\perp)}{2} & 0 \\ 0 & -f'_\perp + \frac{3(f''_\parallel + f''_\perp)}{2} \end{pmatrix}, \quad (\text{S42})$$

$$\mathcal{H}_{LO/TO,\Gamma}^{AB} = \begin{pmatrix} \frac{f'_\perp}{2} - \frac{3(f''_\parallel + f''_\perp)}{4} & 0 \\ 0 & \frac{f'_\perp}{2} - \frac{3(f''_\parallel + f''_\perp)}{4} \end{pmatrix}, \quad (\text{S43})$$

and $\mathcal{V}_{LO/TO,\Gamma}^\alpha$ describe the onsite intra-atomic potential:

$$\mathcal{V}_{LO/TO,\Gamma}^{AA} = \begin{pmatrix} f'_\perp + \frac{3(f''_\parallel + f''_\perp)}{2} & 0 \\ 0 & f'_\perp + \frac{3(f''_\parallel + f''_\perp)}{2} \end{pmatrix}, \quad (\text{S44})$$

$$\mathcal{V}_{LO/TO,\Gamma}^{AB} = \begin{pmatrix} \frac{f'_\perp}{2} + \frac{9(f''_\parallel + f''_\perp)}{4} & 0 \\ 0 & \frac{f'_\perp}{2} + \frac{9(f''_\parallel + f''_\perp)}{4} \end{pmatrix}. \quad (\text{S45})$$

In both stackings, the LO/TO modes at Γ in bilayer systems present two couples of degenerate modes, with frequencies:

$$M\omega_{LO/TO,AA}^2(\Gamma) = \begin{cases} 3(f_\parallel + f_\perp) + 3(f''_\parallel + f''_\perp) & \text{(double degenerate),} \\ 3(f_\parallel + f_\perp) + 2f'_\perp & \text{(double degenerate),} \end{cases} \quad (\text{S46})$$

$$M\omega_{LO/TO,AB}^2(\Gamma) = \begin{cases} 3(f_\parallel + f_\perp) + f'_\perp + \frac{3}{2}(f''_\parallel + f''_\perp) & \text{(double degenerate),} \\ 3(f_\parallel + f_\perp) + 3(f''_\parallel + f''_\perp) & \text{(double degenerate).} \end{cases} \quad (\text{S47})$$

DYNAMICAL MATRIX IN TWISTED BILAYERS

In the above section, we have summarized the effective $\mathbf{k} \cdot \mathbf{p}$ model identifying, for each phonon mode under investigation, the inter-layer elastic force terms and the onsite intra-atomic potentials. A compact view of such local potential is summarized in Table S1 for the relevant degenerate modes LO/LA at the K point, LO/TO modes at the Γ point, and TO at the K point.

Equipped with the knowledge of the role of the interlayer coupling for the characteristic bilayer structures AA and AB, we can now estimate the dynamical matrix for twisted bilayer systems within the framework of a continuum model.

The analysis follows slightly different procedures for each mode, accounting for the different characteristic vectors (K vs. Γ), and for the different size of the Hilbert space [doublet modes for LO/LA(K) and LO/TO(Γ) vs. single non degenerate mode for TO(K)]

Dirac LO/LA modes at the K point

The continuum model for the phonon Dirac spinor associated with the LO/LA modes at the K points follows a standard approach as employed for the electronic dispersion. Within this framework, we consider first two decoupled single-layer systems in the AA stacking, upon which we apply a twist with angle θ . Such geometric configuration defines three characteristic momenta $\mathbf{Q}_1 = k_\theta(0, 1)$, $\mathbf{Q}_2 = k_\theta(\sqrt{3}/2, 1/2)$, $\mathbf{Q}_3 = k_\theta(-\sqrt{3}/2, 1/2)$, where $k_\theta = 2k_{\text{BZ}} \sin(\theta/2)$, k_{BZ} being the absolute value of the momentum of the Brillouin zone edge. The \mathbf{Q}_ν momenta rule the relevant tunneling processes between layers α and β by means of the interlayer couplings:

$$T^{\alpha\beta}(\mathbf{r}) = \bar{t} \sum_{\nu} T_{\nu}^{\alpha\beta} e^{i\mathbf{Q}_\nu \cdot \mathbf{r}}, \quad (\text{S48})$$

LO/LA modes at K				
stacking	$V_{A,1}$	$V_{B,1}$	$V_{A,2}$	$V_{B,2}$
AA	$f'_\perp + 3(f''_\parallel + f''_\perp)/2$	$f'_\perp + 3(f''_\parallel + f''_\perp)/2$	$f'_\perp + 3(f''_\parallel + f''_\perp)/2$	$f'_\perp + 3(f''_\parallel + f''_\perp)/2$
AB	$f'_\perp + 3(f''_\parallel + f''_\perp)/2$	$3(f''_\parallel + f''_\perp)$	$3(f''_\parallel + f''_\perp)$	$f'_\perp + 3(f''_\parallel + f''_\perp)/2$
BA	$3(f''_\parallel + f''_\perp)$	$f'_\perp + 3(f''_\parallel + f''_\perp)/2$	$f'_\perp + 3(f''_\parallel + f''_\perp)/2$	$3(f''_\parallel + f''_\perp)$

LO/TO modes at Γ				
stacking	$V_{x,1}$	$V_{y,1}$	$V_{x,2}$	$V_{y,2}$
AA	$f'_\perp + 3(f''_\parallel + f''_\perp)/2$	$f'_\perp + 3(f''_\parallel + f''_\perp)/2$	$f'_\perp + 3(f''_\parallel + f''_\perp)/2$	$f'_\perp + 3(f''_\parallel + f''_\perp)/2$
AB	$f'_\perp/2 + 9(f''_\parallel + f''_\perp)/4$	$f'_\perp/2 + 9(f''_\parallel + f''_\perp)/4$	$f'_\perp/2 + 9(f''_\parallel + f''_\perp)/4$	$f'_\perp/2 + 9(f''_\parallel + f''_\perp)/4$
BA	$f'_\perp/2 + 9(f''_\parallel + f''_\perp)/4$	$f'_\perp/2 + 9(f''_\parallel + f''_\perp)/4$	$f'_\perp/2 + 9(f''_\parallel + f''_\perp)/4$	$f'_\perp/2 + 9(f''_\parallel + f''_\perp)/4$

TO modes at K		
stacking	V_1	V_2
AA	$f'_\perp + 3(f''_\parallel + f''_\perp)/2$	$f'_\perp + 3(f''_\parallel + f''_\perp)/2$
AB	$f'_\perp/2 + 9(f''_\parallel + f''_\perp)/4$	$f'_\perp/2 + 9(f''_\parallel + f''_\perp)/4$
BA	$f'_\perp/2 + 9(f''_\parallel + f''_\perp)/4$	$f'_\perp/2 + 9(f''_\parallel + f''_\perp)/4$

TABLE S1. Onsite atomic potentials in different stacking orders of bilayer systems for modes LO/LA at the K point LO/TO at the Γ point, and TO at the K point. For the LO/LA modes, the potential is specified for each sublattice of each layer; for the LO/TO modes is specified for x -, y -eigenvectors in Eq. (S6) of each layer; for the TO mode at K is specified for the TO eigenvector in Eq. (S8) in each layer.

where as usual (assuming translational invariance with respect to the relative shift of the two layers)

$$\hat{T}_1 = \begin{pmatrix} 1 & 1 \\ 1 & 1 \end{pmatrix}, \quad \hat{T}_2 = \begin{pmatrix} e^{-2\pi i/3} & 1 \\ e^{2\pi i/3} & e^{-2\pi i/3} \end{pmatrix}, \quad \hat{T}_3 = \begin{pmatrix} e^{2\pi i/3} & 1 \\ e^{-2\pi i/3} & e^{2\pi i/3} \end{pmatrix}. \quad (\text{S49})$$

Following the procedure in Ref. [6], the parameter

$$\bar{t} = \sqrt{t_{AA,i}^2 + t_{AB,i}^2}, \quad (\text{S50})$$

is here an effective energy scale obtained by interpolating the AA and the AB/BA interlayer coupling matrices $\mathcal{H}_{LO/LA}^{AA}$ and $\mathcal{H}_{LO/LA}^{AB}$.

More in particular, following a standard procedure based on a perturbation analysis, using Eqs. (S25)-(S26). we get:

$$t_{AA,LO/LA}(K) = -\frac{f'_\perp}{3}, \quad (\text{S51})$$

$$t_{AB,LO/LA}(K) = -\frac{1}{2}(f''_\parallel - f''_\perp). \quad (\text{S52})$$

Besides the interlayer tunnelling processes, the interlayer elastic coupling between the twisted layers gives rise for each mode to local atomic potentials which are described by the diagonal matrices \mathcal{V}_α^{AA} and \mathcal{V}_α^{AB} , \mathcal{V}_α^{BA} , as they are summarized in Table S1 for the AA and AB structures. In twisted bilayer systems, these potentials can be expanded in reciprocal lattice vectors, in the same way as electrostatic potentials are incorporated into the continuum model of the electron band structure of twisted bilayer graphene[35].

More in particular, for each mode α we can define an average potential \bar{V}_α^{AB} and a potential difference ΔV_α^{BA} for the AB and BA structures,

$$\bar{V}_\alpha^{AB} = \frac{V_\alpha^{AB} + V_\alpha^{BA}}{2}, \quad (\text{S53})$$

$$\Delta V_\alpha^{AB} = \frac{V_\alpha^{AB} - V_\alpha^{BA}}{2}. \quad (\text{S54})$$

Furthermore we can define a potential difference between the average potential in the AA and AB regions:

$$\Delta V_\alpha = V_\alpha^{AA} - \bar{V}_\alpha^{AB}. \quad (\text{S55})$$

Such difference between AA and AB regions can be described in terms of moiré harmonics. Expanding into the first star of moiré reciprocal lattice vectors, we obtain:

$$V_\alpha(\vec{r}) = \frac{\Delta V_\alpha}{9} \sum_{i=1,2,3} \cos(\vec{G}_i \vec{r}). \quad (\text{S56})$$

In similar way, the layer dependent modulation of the potentials at the AB and BA regions can be written as:

$$\Delta V_\alpha(\vec{r}) = \pm \frac{2\Delta V_\alpha^{AB}}{3\sqrt{3}} \sum_{i=1,2,3} \sin(\vec{G}_i \vec{r}) \quad (\text{S57})$$

The potentials in Eqs. (S56)-(S57) can be incorporated into a continuum model in the same way as the electrostatic potential are added to the electronic continuum model of twisted bilayer graphene.[35] We keep only the first star of reciprocal lattice vectors, and include these potentials into the continuum model in a similar way to the inclusion of the (scalar but sublattice independent) Hartree potential in Ref. [35].

The full phonon dispersion of the LO/LA modes in the reduced moiré Brillouin zone can be thus computed, as shown for instance in Fig. 2a,b of the main text. A comparison between the LO/LA dispersion in the twisted case with $\theta = 4^\circ$ and the reference case of two decoupled layers is shown in Fig. S1. The Dirac bands (marked in red color) are easily identified. One can notice two main features: an overall upwards energy shift $\Delta\omega_{LO/LA}$ of the main dispersion, of about $\sim 1.8 \text{ cm}^{-1}$; and a renormalization of the linear Dirac dispersion, just like for the electronic case. For given angle, we evaluate the coefficient v^* of the linear dispersion $\hbar\omega_{LO/LA}(\vec{k}) = \hbar\omega_{LO/LA}(K) \pm v^*|\vec{p}|$ of the Dirac mode in the twisted case in comparison with the linear coefficient v of the uncoupled single-layer. The parameter $R = v^*/v$ provides thus the “renormalization” band factor of the twisted Dirac phonons dispersion, in similar was as shown in the inset of Fig. 4 in Ref. [5]. The angle dependence of the renormalization band factor is shown in Fig. 2c of the main text, showing a remarkable trend toward flat Dirac bands for $\theta \lesssim 2^\circ$. Also interesting, is the analysis of the phonon band-shift $\Delta\omega_{LO/LA}$, reported in Fig. S2, which shows a negligible dependence on θ for large twist angles, but a sizable drop at low angle, in the region where the band renormalization is also more marked. Such angle dependence of the phonon band-shift $\Delta\omega_{LO/LA}$, is expected to be reflected in an observable angle-dependence mode softening.

If we neglect for the moment the role of the onsite potentials, we can use a perturbative analysis of the interlayer tunneling terms (see for instance Ref. 5) in order to obtain an estimate of the first “magic” angle at which the phonon dispersion of the twisted bilayer vanishes.

For the case of the Dirac-like phonons LO/LA at the K point, such condition occurs when

$$2 \sin\left(\frac{\bar{\theta}_{LO/LA}}{2}\right) = \frac{3}{4\pi} \frac{\sqrt{3}\bar{t}^2}{V} = \frac{\sqrt{3}}{\pi(f_{\parallel} - f_{\perp})} \sqrt{3 \left[(f'_{\perp})^2 + \frac{9(f''_{\parallel} - f''_{\perp})^2}{4} \right]}. \quad (\text{S58})$$

Using the force-constant parameters extracted from the comparison with ab-initio calculations (see next Section), this equation gives $\bar{\theta}_{LO/LA}(K) \approx 2.1^\circ$.

High-energy TO modes at the K point

The TO phonons at the K point in twisted systems can also be described as a variation of the continuum model discussed in Ref. 6, where we expand the dynamical matrix in Bloch wavefunctions at each layer. Just as in the previous case, the interlayer scattering is still governed by the three characteristic momenta $\mathbf{Q}_1 = k_\theta(0, 1)$, $\mathbf{Q}_2 = k_\theta(\sqrt{3}/2, 1/2)$, $\mathbf{Q}_3 = k_\theta(-\sqrt{3}/2, 1/2)$. With respect to the LO/LA modes, there are however two main differences. One one hand, the phonon dispersion in the single-layer does not obey to a linear behavior but to a quadratic one as shown in Eq.(S33). On the other hand, as this mode in single-layer is not degenerate, the 2×2 spinor structure of Eq. (S49) is lifted, and for each momentum only one wave function per layer is needed. The terms which define the interlayer tunneling are thus reduced to 1×1 numbers, as in Eq. (S34)-(S35). A block state

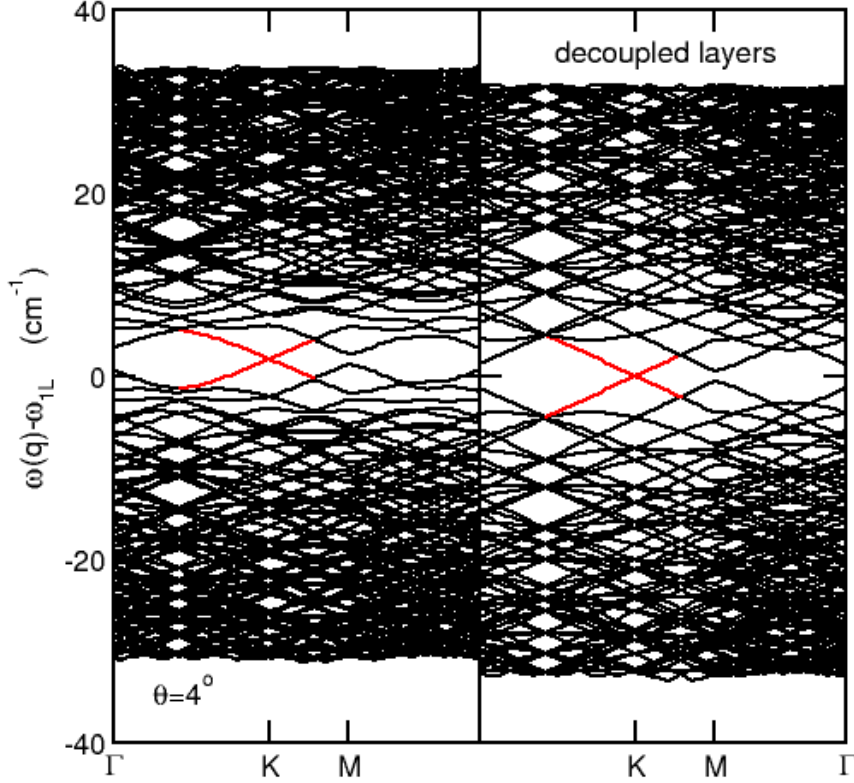


FIG. S1. Band dispersion for the LO/LA modes in the reduced moiré Brillouin zone for twisted bilayer case at $\theta = 4^\circ$ (left panel) and for the reference case of the decoupled layers (right panel). Marked in red is the linear Dirac-like dispersion.

in one layer is coupled by these terms to three Bloch states in the second layers, and the three terms just acquire a phase modulation, $e^{i\phi_j}$, $j = 1, 2, 3$ (see Ref. 36 for a related approach to the electronic states in twisted homo-bilayer dichalcogenides). Finally we include the intra-layer sublattice potentials V_1, V_2 as shown in Table S1. Just as in the case of the Dirac LO/LA modes, these local potentials are expanded using the first star of reciprocal lattice vectors.

The phonon dispersion so computed is shown in panels d-e of Fig. 2 of the main text. Also in this case, a renormalization band factor can be evaluate by the ratio of the quadratic dispersion $\hbar\omega_{TO}(\vec{k}) = \hbar\omega_{TO}(K) + \alpha^* |\vec{p}|^2$ in the twisted bilayer and in the single layer cases, $R = \alpha^*/\alpha$. The angle dependence of the such renormalization band factor is also shown in panel f of Fig. 2 of the main text, and the angle dependence of the band-shift $\Delta\omega_{TO}$ for this mode in Fig. S2.

Also for the TO modes at the K point, using the same perturbative approach for the interlayer tunneling, we can provide a qualitative estimate of the magic angle were the positive quadratic dispersion at K is renormalized to zero. Using the appropriate expression for a quadratic dispersion we find:

$$2 \sin\left(\frac{\bar{\theta}_{TO}}{2}\right) = \frac{3}{4\pi} \times \sqrt{\frac{2\sqrt{3} \left| f'_\perp + \frac{3(f'_\perp - f''_\parallel)}{2} \right| (f_\parallel - f_\perp)}{f_\parallel f_\perp}}. \quad (\text{S59})$$

Note that this result depends only on the prefactor of the quadratic dispersion of the TO mode of a monolayer, and on the set of interlayer force-constant parameters which describes the force between layers in the AA structure, as

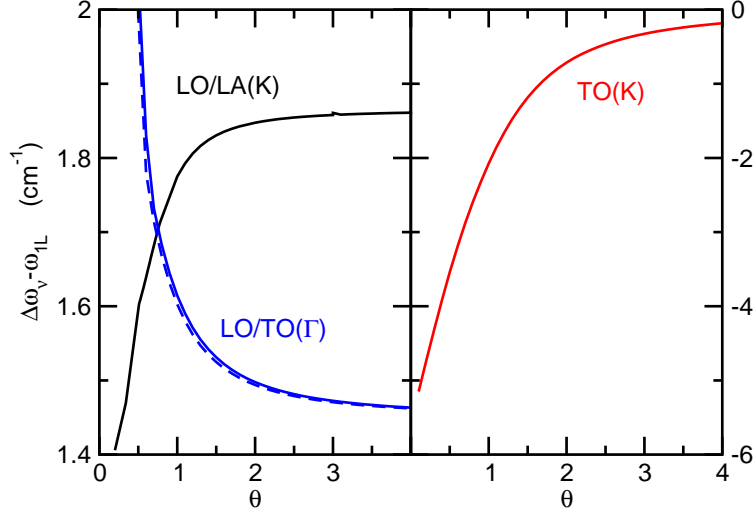


FIG. S2. Angle dependence of the band shift $\Delta\omega_\nu$ for the relevant modes $\nu = LO/LA(K), TO(K), LO/TO(\Gamma)$. For the LO/TO modes, the blue solid line refers to the even symmetry, while the dashed line to the odd symmetry.

defined in Eq.(S34).

Using the force-constant parameters extracted from the comparison with ab-initio calculations, we get $\bar{\theta}_{TO}(K) \approx 1.0^\circ$.

High-energy LO/TO modes at the Γ point

The analysis of the twisting on the LO/TO modes at the Γ point is somehow much simpler than the previous cases discussed for phonons at the K point. The phonons at the Γ point in the individual layers of a twisted bilayer are indeed mapped onto the Γ point of the twisted bilayer Brillouin zone, unlike the modes at the K point, which are instead mapped onto the K or K' point of the twisted bilayer Γ point, depending on the layer index. Moreover, as shown in Eqs. (S42), (S43), (S44), (S45), and in Table S1, all the interlayer coupling terms are just multiple of the unit matrix in the 2×2 space, as specified in Eqs. (S42)-(S43). Hence, the LO and TO modes can be treated independently. The continuum model for the phonons at the Γ point can be written in terms of Bloch waves defined on the reciprocal lattices for each layer, where the two lattices lie on top of each other, unlike the case of the modes at K , where the two reciprocal lattices are displaced with respect to each other.[5] A similar model has been employed for electrons near the Γ point of the valence band in transition metal dichalcogenides.[38, 40] Furthermore, the interlayer coupling terms allow for the separation of the two LO and the two TO modes into even and odd combinations which also are decoupled, so that the continuum model for the dynamical matrix of the phonons at Γ can be split into four independent blocks.

Using such procedure, the computed phonon dispersion and the angle dependence of the renormalization band factor for the TO modes close to the Γ point are shown in panels g-i of Fig. 2 of the main text. We also show in Fig. S2 the angle dependence of the band-shifts $\Delta\omega_{LO/TO}$ of these modes for both even and odd symmetries. Note that, since LO and TO are degenerate at the Γ point, a similar band-shift applies for both LO and TO phonon dispersions.

Obeying to the above simplifications, also the estimates of magic angles where the dispersion of the TO/LO modes at the Γ point is renormalized to zero ($R \rightarrow 0$) is significantly simplified.

Since, as discussed above, the continuum model for the phonons at Γ can be split into four independent hamiltonian blocks, corresponding to even and odd layer combinations, we obtain four magic angles, one for each LO vs. TO and even vs. odd combinations. Using the interlayer coupling reported in Eqs. (S42)-(S43), the quadratic dispersion of Eq.(S41), and using non local coupling between Bloch waves separated by a reciprocal lattice vector in the first star,

the perturbation theory results in the following relations:

$$\begin{aligned} 2 \sin\left(\frac{\bar{\theta}}{2}\right) &= \frac{\sqrt{3}}{4\pi} \sqrt{\frac{|\tilde{f}_1 \pm \tilde{f}'_1|}{v_2^{LO}}}, \\ 2 \sin\left(\frac{\bar{\theta}}{2}\right) &= \frac{\sqrt{3}}{4\pi} \sqrt{\frac{|\tilde{f}_1 \pm \tilde{f}'_1|}{v_2^{TO}}}, \end{aligned} \quad (\text{S60})$$

where:

$$\begin{aligned} \tilde{f}_1 &= \frac{f'_\perp - \frac{3}{2}(f''_\parallel + f''_\perp)}{18}, \\ \tilde{f}'_1 &= \frac{-3f'_\perp + \frac{3}{2}(f''_\parallel + f''_\perp)}{18}, \\ v_2^{LO} &= \frac{f_\perp(3f_\parallel + f_\perp)}{8(f_\parallel + f_\perp)}, \\ v_2^{TO} &= \frac{f_\parallel(f_\parallel + 3f_\perp)}{8(f_\parallel + f_\perp)}. \end{aligned} \quad (\text{S61})$$

Using the force-constant parameters extracted from the comparison with ab-initio calculations, we find $\bar{\theta}_{LO}(\Gamma, +) \approx 0.44^\circ$, $\bar{\theta}_{TO}(\Gamma, +) \approx 0.42^\circ$, $\bar{\theta}_{LO}(\Gamma, -) \approx 0.83^\circ$, $\bar{\theta}_{TO}(\Gamma, -) \approx 0.79^\circ$.

MAPPING AB-INITIO CALCULATIONS ONTO FORCE-CONSTANT MODEL

In order to achieve a realistic modelling of the lattice dynamics in twisted bilayer graphene, we use ab-initio calculations in order to extract the appropriate parameters for the force-constant model.

Density functional theory calculations (DFT) were performed using Quantum Espresso (QE)[34, 53, 54]. For the electronic calculations, we use the Generalized Gradient Approximation (GGA), specifically, the functional of Perdew, Burke and Ernzerhof [55]. We set the energy cutoff for the wavefunctions to 240 Ry and the cutoff for the density to 1400 Ry. In order to obtain the correct value for the interlayer spacing in the case of bilayer graphene, we use the Grimme approximation[56]. The Brillouin zone was sampled using the Monkhorst–Pack scheme [57] with a grid of $32 \times 32 \times 1$ k-points. We have optimized the lattice vectors and relaxed the atomic positions to forces lower than 1 eV/Å. The phonon band structure was calculated using Density Functional Perturbation Theory (DFPT)[58] as implemented in QE.

The force-constant (FC) model here employed for the phonon dispersion in bilayer graphene depends on five independent elastic parameters, i.e. f_\parallel , f_\perp , f'_\perp , f''_\parallel , and f''_\perp . Given the pivotal role in our discussion of the Dirac-like LO/LA modes at the K point of single-layer and bilayer structures, we calibrate our FC parameters in order to reproduce in the best way these Dirac-like features.

A first crucial feature is in the single-layer the Dirac-like linear dispersion of the LO/LA modes at the K point,

$$\hbar\omega_{LO/LA}(\vec{k}) = \hbar\omega_{LO/LA}(K) \pm v|\vec{p}|, \quad (\text{S62})$$

where $\vec{p} = \vec{k} - K$. Our DFT calculations find

$$v = 7.25 \times 10^4 \text{ cm/s} = 4.77 \text{ meV \AA}. \quad (\text{S63})$$

Further relevant ab-initio inputs are the LO/LA frequencies in the single-layer as well as AA and AB stackings. Their values are reported in Table S2

These first-principle inputs can be now employed in order to estimate proper force-constant parameters. More in details, from the relation:

$$M\omega_{LO/LA}^2(K) = \frac{3}{2}(f_\parallel + f_\perp), \quad (\text{S64})$$

we get the value of the linear combination $f_\parallel + f_\perp$:

$$f_\parallel + f_\perp = 43.85 \text{ eV/\AA}^2. \quad (\text{S65})$$

1L	AA	AB
1215.34*	1214.78*	1215.41
	1217.41*	1215.54*
		1216.26

TABLE S2. Ab-initio LO/LA phonon frequencies at the K point in units of cm^{-1} . Frequencies marked with (*) are double degenerate.

The first-principles value of the Dirac velocity v of these modes close to K provide further analytical constraints. From Eq. (S12), which refers to the dynamical matrix, we can obtain an analytical expression for v :

$$v = \sqrt{\frac{3(f_{\parallel} + f_{\perp})}{2} \frac{f_{\parallel} - f_{\perp}}{f_{\parallel} + f_{\perp}} \frac{\hbar a}{4\sqrt{3}}}, \quad (\text{S66})$$

Using these inputs we can determine thus the values of the in-plane force-constant parameters f_{\parallel} and f_{\perp} .

The interlayer force-constant parameters f'_{\perp} , f''_{\parallel} , and f''_{\perp} can be estimated from the spectrum of the LO/LA modes at the K point in the AA and AB structures. Using Eqs. (S30), from the splitting of the computed frequencies of the Dirac LO/LA modes in the AA structure, we can extract the value of $2f'_{\perp}$. In similar way, using Eqs. (S31), we can extract the linear combination $f''_{\parallel} - f''_{\perp}$ from the splitting of the single-degenerate LO/LA levels at K in the AB structure. In order to have a complete set of force-constant parameters, we have to further extract from the ab-initio calculations the linear combination $f''_{\parallel} + f''_{\perp}$. This can be obtained, using Eqs. (S9) and (S30), by comparing the frequency shift of the symmetric LO/LA modes in the AA bilayer with respect to the reference frequency of the LO/LA modes in the single-layer case. The force-constant parameters so extracted from the ab-initio input are listed in Table S3.

It is worth to mention that, while the parameters f_{\parallel} , f_{\perp} , f'_{\perp} , and the linear combination $f''_{\parallel} - f''_{\perp}$ are extracted in a compelling way from the analysis of the LO/LA modes at the K point in single-layer and bilayer structure, the determination of the last condition, namely $f''_{\parallel} + f''_{\perp}$, is less univocally. As an alternative procedure, we could estimate the linear combination $f''_{\parallel} + f''_{\perp}$, using Eq. (S31), from the analysis of the the relative frequency shift of the LO/LA modes in the AB bilayer with respect to the reference frequency of the LO/LA modes in the single-layer case. Along this derivation, one would extract slightly different values of f''_{\parallel} , f''_{\perp} , namely $f''_{\parallel} = 0.070 \text{ eV}/\text{\AA}^2$, $f''_{\perp} = 0.039 \text{ eV}/\text{\AA}^2$. Note however that such slight uncertainty on the quantity $f''_{\parallel} - f''_{\perp}$ does not affect sensibly the twisted phonon dispersion since the relevant interlayer tunneling processes, for the LO/LA modes at the K point, as well as for the TO at K and TO/LO at Γ , are essentially ruled [see Eqs. (S51), (S52) (S34), (S35), (S42), and (S43)] only by the parameters f'_{\perp} , and $(f''_{\parallel} - f''_{\perp})$ which can be determined without ambiguity from the first-principle calculations. In Fig. S3 we show the phonon dispersions for $\theta = 1.05^{\circ}, 4^{\circ}$ and the angle dependence of the band renormalization factor R for the force-constant parameter set with $f''_{\parallel} = 0.070 \text{ eV}/\text{\AA}^2$, $f''_{\perp} = 0.039 \text{ eV}/\text{\AA}^2$. Both features appear essentially identical to the results shown in the main text with the parameters listed in Table S3.

f_{\parallel}	f_{\perp}	f'_{\perp}	f''_{\parallel}	f''_{\perp}
23.882	19.973	-0.143	0.090	0.059

TABLE S3. Force-constant parameters extracted from ab-initio calculations, in units of $\text{eV}/\text{\AA}^2$.

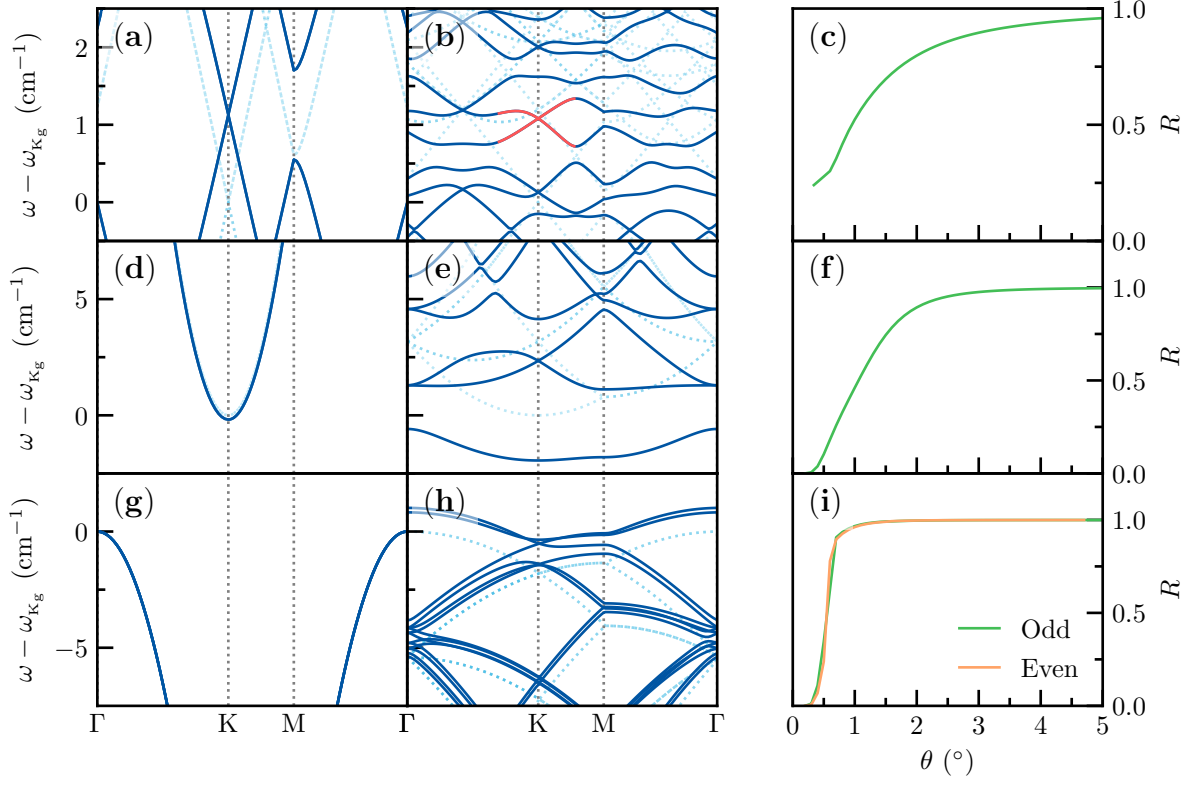


FIG. S3. (Phonon dispersion in the moiré Brillouin zone for $\theta = 4.0^\circ$ and $\theta = 1.05^\circ$ (left and middle columns) and phonon band renormalization factor R as function of the twist angle θ computed by using the force-parameter set $f_{\parallel} = 23.882 \text{ eV}/\text{\AA}^2$, $f_{\perp} = 19.973 \text{ eV}/\text{\AA}^2$, $f'_{\perp} = -0.143 \text{ eV}/\text{\AA}^2$, $f''_{\parallel} = 0.070 \text{ eV}/\text{\AA}^2$, $f'_{\perp} = 0.039 \text{ eV}/\text{\AA}^2$.

* josilgui@gmail.com

† paco.guinea@gmail.com

- [1] Y. Cao, V. Fatemi, S. Fang, K. Watanabe, T. Taniguchi, E. Kaxiras, and P. Jarillo-Herrero, *Nature* **556**, 43 (2018).
- [2] Y. Cao, V. Fatemi, A. Demir, S. Fang, S. L. Tomarken, J. Y. Luo, J. D. Sanchez-Yamagishi, K. Watanabe, T. Taniguchi, E. Kaxiras, R. C. Ashoori, and P. Jarillo-Herrero, *Nature* **556**, 80 (2018).
- [3] E. Suárez Morell, J. D. Correa, P. Vargas, M. Pacheco, and Z. Barticevic, *Phys. Rev. B* **82**, 121407 (2010).
- [4] G. De Trambly Laissardière, D. Mayou, and L. Magaud, *Nano Lett.* **10**, 804 (2010).
- [5] R. Bistritzer and A. H. MacDonald, *Proceedings of the National Academy of Sciences* **108**, 12233 (2011).
- [6] J. M. B. Lopes dos Santos, N. M. R. Peres, and A. H. Castro Neto, *Phys. Rev. Lett.* **99**, 256802 (2007).
- [7] E. J. Mele, *Phys. Rev. B* **84**, 235439 (2011).
- [8] A. I. Cocemasov, D. L. Nika, and A. A. Balandin, *Phys. Rev. B* **88**, 035428 (2013).
- [9] A. Jorio and L. G. Cançado, *Solid St. Commun.* **175-176**, 3 (2023).
- [10] F. Wu, A. H. MacDonald, and I. Martin, *Phys. Rev. Lett.* **121**, 257001 (2018).
- [11] B. Lian, Z. Wang, and B. A. Bernevig, *Phys. Rev. Lett.* **122**, 257002 (2019).
- [12] F. Wu, E. Hwang, and S. Das Sarma, *Phys. Rev. B* **99**, 165112 (2019).
- [13] M. Angeli, E. Tosatti, and M. Fabrizio, *Phys. Rev. X* **9**, 041010 (2019).
- [14] M. Angeli and M. Fabrizio, *The European Physical Journal* **135**, 630 (2020).
- [15] A. Blason and M. Fabrizio, *Phys. Rev. B* **106**, 235112 (2022).
- [16] A. C. Ferrarini and J. Robertson, *Phys. Rev. B* **61**, 14095 (2000).
- [17] S. Piscanec, M. Lazzeri, F. Mauri, A. C. Ferrari, and J. Robertson, *Phys. Rev. Lett.* **93**, 185503 (2004).
- [18] A. C. Ferrari, J. C. Meyer, V. Scardaci, C. Casiraghi, M. Lazzeri, F. Mauri, S. Piscanec, D. Jiang, K. S. Novoselov, S. Roth, and A. K. Geim, *Phys. Rev. Lett.* **97**, 187401 (2006).
- [19] D. M. Basko, *Phys. Rev. B* **76**, 081405 (2007).
- [20] D. M. Basko, *Phys. Rev. B* **78**, 125418 (2008).
- [21] M. Rosendo López, F. Peñaranda, J. Christensen, and P. San-Jose, *Phys. Rev. Lett.* **125**, 214301 (2020).
- [22] Y. Deng, M. Oudich, N. J. Gerard, J. Ji, M. Lu, and Y. Jing, *Phys. Rev. B* **102**, 180304 (2020).
- [23] M. J. Matthews, M. A. Pimenta, G. Dresselhaus, M. S. Dresselhaus, and M. Endo, *Phys. Rev. B* **59**, R6585 (1999).
- [24] C. Thomsen and S. Reich, *Phys. Rev. Lett.* **85**, 5214 (2000).
- [25] L. Zhang and Q. Niu, *Phys. Rev. Lett.* **112**, 085503 (2014).
- [26] L. Zhang and Q. Niu, *Phys. Rev. Lett.* **115**, 115502 (2015).
- [27] H. Zhu, J. Yi, M.-Y. Li, J. Xiao, L. Zhang, C.-W. Yang, R. A. Kaindl, L.-J. Li, Y. Wang, and X. Zhang, *Science* **359**, 579 (2018).
- [28] H. Chen, W. Zhang, Q. Niu, and L. Zhang, *2D Mater.* **6**, 012002 (2019).
- [29] H. Rostami, F. Guinea, and E. Cappelluti, *Phys. Rev. B* **105**, 195431 (2022).
- [30] N. Suri, C. Wang, Y. Zhang, and D. Xiao, *Nano Lett.* **21**, 10026 (2021).
- [31] I. Maity, A. A. Mostofi, and J. Lischner, *Phys. Rev. B* **105**, L041408 (2022).
- [32] See Supplementary Material.
- [33] Note that in order to properly estimate the interlayer force-constant parameters an inspection of the eigenvectors of the Dirac modes in the AA structure, besides their energies, is needed.
- [34] P. Giannozzi, O. Baseggio, P. Bonfà, D. Brunato, R. Car, I. Carnimeo, C. Cavazzoni, S. de Gironcoli, P. Delugas, F. Ferrari Ruffino, A. Ferretti, N. Marzari, I. Timrov, A. Urru, and S. Baroni, *The Journal of Chemical Physics* **152**, 154105 (2020).
- [35] F. Guinea and N. R. Walet, *Proceedings of the National Academy of Sciences* **115**, 13174 (2018).
- [36] F. Wu, T. Lovorn, E. Tutuc, I. Martin, and A. H. MacDonald, *Phys. Rev. Lett.* **122**, 086402 (2019).
- [37] S. Carr, S. Fang, and E. Kaxiras, *Nature Reviews Materials* **5**, 748 (2020).
- [38] Y. Zhang, T. Liu, and L. Fu, *Phys. Rev. B* **103**, 155142 (2021).
- [39] N. R. Walet and F. Guinea, *Phys. Rev. B* **103**, 125427 (2021).
- [40] M. Angeli and A. MacDonald, *Proc. Nat. Acad. Sci.* **118**, e2021826118 (2021).
- [41] H. Wang, Y. Wang, X. Cao, M. Feng, and G. Lan, *Journal of Raman Spectroscopy* **40**, 1791 (2009).
- [42] L. M. Malard, D. C. Elias, E. S. Alves, and M. A. Pimenta, *Phys. Rev. Lett.* **101**, 257401 (2008).
- [43] P. Gava, M. Lazzeri, A. M. Saitta, and F. Mauri, *Phys. Rev. B* **80**, 155422 (2009).
- [44] A. B. Kuzmenko, L. Benfatto, E. Cappelluti, I. Crassee, D. van der Marel, P. Blake, K. S. Novoselov, and A. K. Geim, *Phys. Rev. Lett.* **103**, 116804 (2009).
- [45] T.-T. Tang, Y. Zhang, C.-H. Park, B. Geng, C. Girit, Z. Hao, M. Martin, A. Zettl, M. Crommie, S. Louie, S. Y.R., and F. Wang, *Nature Nanotech.* **5**, 32 (2009).
- [46] E. Cappelluti, L. Benfatto, M. Manzardo, and A. B. Kuzmenko, *Phys. Rev. B* **86**, 115439 (2012).
- [47] A. Jorio, M. Kasperczyk, N. Clark, E. Neu, P. Maletinsky, A. Vijayaraghavan, and L. Novotny, *Nano Letters* **14**, 5687 (2014).
- [48] V. N. Popov, *Journal of Raman Spectroscopy* **49**, 31 (2018).
- [49] A. García-Ruiz, J. J. P. Thompson, M. Mucha-Kruczyński, and V. I. Fal'ko, *Phys. Rev. Lett.* **125**, 197401 (2020).
- [50] K. Chang, Z. Zheng, J. E. Sipe, and J. L. Cheng, *Phys. Rev. B* **106**, 245405 (2022).

- [51] N. Suri, C. Wang, Y. Zhang, and D. Xiao, *Nano Letters* **21**, 10026 (2021).
- [52] I. Maity, A. A. Mostofi, and J. Lischner, *Phys. Rev. B* **105**, L041408 (2022).
- [53] P. Giannozzi, S. Baroni, N. Bonini, M. Calandra, R. Car, C. Cavazzoni, D. Ceresoli, G. L. Chiarotti, M. Cococcioni, I. Dabo, A. D. Corso, S. de Gironcoli, S. Fabris, G. Fratesi, R. Gebauer, U. Gerstmann, C. Gougoussis, A. Kokalj, M. Lazzeri, L. Martin-Samos, N. Marzari, F. Mauri, R. Mazzarello, S. Paolini, A. Pasquarello, L. Paulatto, C. Sbraccia, S. Scandolo, G. Sclauzero, A. P. Seitsonen, A. Smogunov, P. Umari, and R. M. Wentzcovitch, *Journal of Physics: Condensed Matter* **21**, 395502 (2009).
- [54] P. Giannozzi, O. Andreussi, T. Brumme, O. Bunau, M. B. Nardelli, M. Calandra, R. Car, C. Cavazzoni, D. Ceresoli, M. Cococcioni, N. Colonna, I. Carnimeo, A. D. Corso, S. de Gironcoli, P. Delugas, R. A. DiStasio, A. Ferretti, A. Floris, G. Fratesi, G. Fugallo, R. Gebauer, U. Gerstmann, F. Giustino, T. Gorni, J. Jia, M. Kawamura, H.-Y. Ko, A. Kokalj, E. Küçükbenli, M. Lazzeri, M. Marsili, N. Marzari, F. Mauri, N. L. Nguyen, H.-V. Nguyen, A. O. de-la Roza, L. Paulatto, S. Poncé, D. Rocca, R. Sabatini, B. Santra, M. Schlipf, A. P. Seitsonen, A. Smogunov, I. Timrov, T. Thonhauser, P. Umari, N. Vast, X. Wu, and S. Baroni, *Journal of Physics: Condensed Matter* **29**, 465901 (2017).
- [55] J. P. Perdew, K. Burke, and M. Ernzerhof, *Phys. Rev. Lett.* **77**, 3865 (1996).
- [56] S. Grimme, *Journal of Computational Chemistry* **27**, 1787 (2006).
- [57] H. J. Monkhorst and J. D. Pack, *Phys. Rev. B* **13**, 5188 (1976).
- [58] S. Baroni, S. de Gironcoli, A. Dal Corso, and P. Giannozzi, *Rev. Mod. Phys.* **73**, 515 (2001).